

Theory and mitigation of motional eddy current in high-field eddy current shielding

Cite as: J. Appl. Phys. **136**, 024504 (2024); doi: [10.1063/5.0210709](https://doi.org/10.1063/5.0210709)

Submitted: 26 March 2024 · Accepted: 20 June 2024 ·

Published Online: 12 July 2024



View Online



Export Citation



CrossMark

Seung-Kyun Lee^{a),b)}  and Yihe Hua^{c)}

AFFILIATIONS

GE HealthCare Technology & Innovation Center, Niskayuna, New York 12309, USA

^{a)}Author to whom correspondence should be addressed: lee.seungkyun@gmail.com

^{b)}lsk@gehealthcare.com

^{c)}Yihe.Hua@gehealthcare.com

ABSTRACT

Eddy current shielding by a Faraday cage is an effective way to shield alternating-current magnetic fields in scientific instrumentation. In a strong static magnetic field, however, the eddy current in the conductive shield is subject to the Lorentz force, which causes the shield to vibrate. In addition to mechanical issues (e.g., acoustic noise), such vibration induces motional eddy current in the shield that can dominate the original, electromagnetic eddy current to undermine the conductor's shielding capability. In this work, we investigate a method to control motional eddy current by making cut-out patterns in the conductor that follow the electromagnetic eddy current image. This effectively limits the surface current of the plate to a single mode and prevents the proliferation of uncontrolled motion-induced surface currents that disrupts eddy current shielding. After developing a comprehensive theory of magneto-mechanical interaction in a conductive plate, the proposed method was tested on a flat-geometry testbed experiment inside a 3 T magnetic resonance imaging (MRI) magnet. It was found that the magnetic field generated by the motional eddy current was much more localized in space and frequency for a patterned-copper shield compared to a solid copper. The magnetic field of the patterned shield could be accurately predicted from the impedance measurement in the magnet. Implications of our results for improved shielding of gradient fields in high-field MRI are discussed.

© 2024 Author(s). All article content, except where otherwise noted, is licensed under a Creative Commons Attribution-NonCommercial 4.0 International (CC BY-NC) license (<https://creativecommons.org/licenses/by-nc/4.0/>). <https://doi.org/10.1063/5.0210709>

I. INTRODUCTION

Eddy current shielding of time-varying magnetic fields by conductive plates and shells is widely used in scientific instruments as well as everyday electrical devices. The shielding is based on the fact that at sufficiently high frequencies, all conductors develop eddy current to counteract applied magnetic flux changes, effectively preventing time-varying magnetic fields from entering their interior. When a conductive shield is placed inside a strong static magnetic field, as in a modern high-field magnetic resonance imaging (MRI) scanner, the eddy current is subject to Lorentz force, leading to the vibration of the shield. The moving conductor now experiences two kinds of time-varying magnetic fluxes in its frame of reference: (i) the original, externally applied AC magnetic field and (ii) the changing flux as it cuts through the flux lines of the static magnetic field.¹ The latter flux induces its own eddy current, sometimes called motional eddy current.² Depending on the static field and the vibration amplitude, the

motional eddy current can dominate the original, electromagnetic eddy current. In this case, the conductor can no longer provide shielding because the field generated by the motional eddy current can be very different in shape and larger in magnitude than the applied field.

The failure of eddy current shielding in a strong static magnetic field has long been noted in MRI engineering as the time-varying fields generated by the gradient coils in the bore of a cylindrical magnet were found to heat the superconducting coils despite multiple conductive shells in between them.^{3–6} The heating cannot easily be explained without motional eddy current. It should be noted that most modern MRI gradient coils employ self-shielded design where each field-generating (primary) coil unit is paired with a shielding coil on the outside of and connected in series with the primary coil.⁷ This greatly reduces the field reaching the magnet, but the residual “leakage” field can still be substantial, on the order of several milliTesla. This is sufficient to heat the

superconducting magnet absent some degree of passive shielding provided by conductive cylinders in the cryostat.

Given the importance of thermal protection of superconducting coils, much effort has been directed to reducing the motional eddy current, through gradient design,³ additional passive shielding,⁸ warm bore engineering,^{9,10} and magnet reinforcement.¹¹ While promising, most structural methods face an important challenge, that is, limited space between the driving (gradient) coils and the protected structure (magnet). In high-field compact MRI scanners,¹² in particular, any radial space between the gradient and magnet coils comes at a steep cost in terms of manufacturing, performance, and energy consumption/efficiency.¹³

The purpose of this paper is to investigate a new method to reduce and control the motional eddy current, not through purely structural intervention, but by limiting eddy current modes in the conductor through cut-out patterns. The pattern is defined by the ideal eddy current in the high-frequency limit in the absence of vibration. By allowing such eddy current to flow in the conductor, while blocking all other modes orthogonal to this mode, the conductor can support non-motional eddy current that is necessary for shielding,¹⁴ while being less prone to unwanted eddy current in the presence of vibration. We first present a comprehensive theory of magneto-mechanical coupling in inductively driven motion of a conductive plate in a static field. We then demonstrate the proposed method in a flat-geometry testbed experiment at 3 T, using a flat copper plate as a model for a passive shield placed between a gradient coil and an MRI magnet.

II. THEORY

We consider a thin conductive plate with surface conductivity σ_s (Fig. 1) that is horizontally placed on the zx plane, and whose vibration consists of vertical (y -directional) displacement $u(z, x)$ that is time-dependent. A static magnetic field B_0 is applied in the z direction. Surface eddy current induced in the conductor is characterized by a stream function $T(z, x)$, which is related¹⁵ to the surface current $\vec{j}(z, x)$ by $(j_z, j_x) = (\partial T/\partial x, -\partial T/\partial z) = \nabla \times (T\hat{y})$. Choice of a horizontal zx plane is motivated by the typical coordinate system of a horizontal-bore MRI magnet. The conductive plate is subject to time-varying magnetic field $B_{app}(z, x) \hat{y} \cos \omega t$, which induces

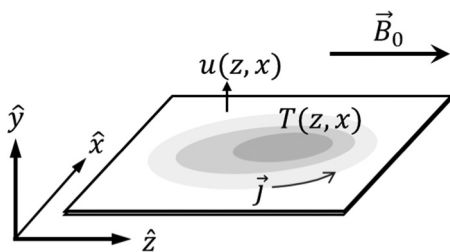


FIG. 1. Definition of the coordinate system and variables. A static magnetic field $\vec{B}_0 = B_0\hat{z}$ is applied parallel to a conductive plate in the zx plane whose vibration is characterized by the vertical displacement $u(z, x)\hat{y}$. The eddy current stream function and the corresponding surface current density are denoted by T and \vec{j} , respectively.

eddy current. If the eddy current completely nulls B_{app} on the surface of the plate, the plate functions as a perfect shield. This will be the case if the plate superconducts, or if the frequency is infinitely high, provided there is no vibration. We will call such an eddy current an eddy image current, whose stream function is denoted as T_{eddyi} [Fig. 2(a)]. At a finite frequency and finite σ_s , the eddy current will deviate from T_{eddyi} . As long as $B_0 = 0$, however, a plate made of a good conductor (e.g., copper or aluminum) with mm-range thickness and tens of cm-range lateral dimensions will still provide good shielding of magnetic fields above a few hundred Hz; the eddy current will be substantially similar to T_{eddyi} in spatial shape. Such a frequency range is important for the thermal protection of MRI magnets.

In the presence of strong B_0 , on the other hand, the surface current can drastically differ from T_{eddyi} , dominated by motional eddy current. This results in passive shielding failure; in fact, a conductive plate can amplify the applied field. In MRI, this phenomenon has been linked to excessive helium boil-off in the magnet cryostat induced by switched gradient fields.^{1-3,16} The goal of this section is to develop a physical theory to calculate the *total* eddy current in response to the applied field B_{app} that includes the motional eddy current. We will primarily work in the frequency domain at angular frequency $\omega = 2\pi f$.

A. Magneto-mechanical coupled equations for a conductive plate in a static magnetic field

Detailed derivation of the coupled equations, namely, the equation of motion and the circuit equation, is given in Appendix A. Below we describe the equations and discuss their properties. We will use script-font characters $\mathcal{A}, \mathcal{B}, \dots$ to denote the linear operators acting on scalar fields defined in the zx plane. The equation of motion of the plate under the influence of the Lorentz force can be written as the following:

$$\mathcal{A}u = \mathcal{B}T, \quad (1)$$

where

$$\mathcal{A} \equiv -\mathcal{F}_M - \rho_m \omega^2 \quad (2)$$

is a mechanical force operator acting on $u(z, x)$ that includes the plate's restoring and damping forces (both captured in \mathcal{F}_M) as well as the inertia term. Here, ρ_m is the surface mass density in (kg/m^2) and the operator \mathcal{F}_M is given, for a thin elastic plate, by¹⁷

$$\mathcal{F}_M u = -D\nabla^4 u - i\omega\lambda u, \quad (3)$$

where D and λ are the bending stiffness and damping coefficient, respectively. The operator \mathcal{B} represents the Lorentz force per unit area acting on T and is given by (see Appendix A)

$$\mathcal{B} \equiv B_0 \frac{\partial}{\partial z}. \quad (4)$$

The circuit equation that governs the evolution of the surface current, in the presence of motional electromotive force (EMF) and

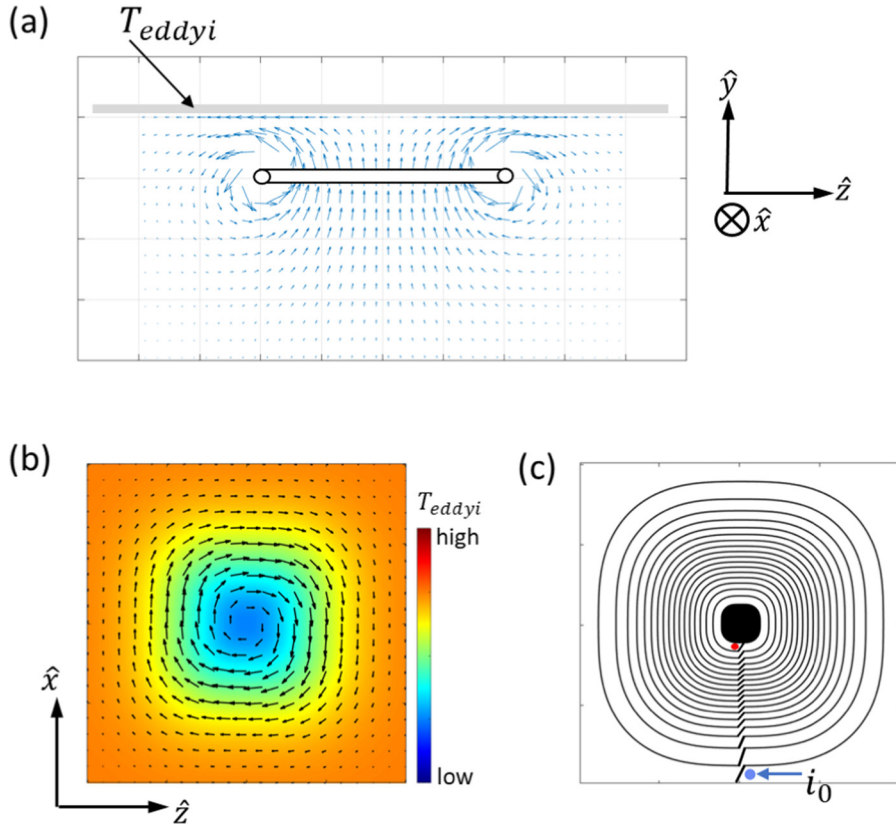


FIG. 2. Eddy image current and its discretization. (a) In the high-frequency limit, the eddy current in a conductive plate (gray horizontal bar) prevents the penetration of an applied magnetic field generated by a driving coil (black-outlined horizontal bar). Such eddy current, whose stream function is denoted as T_{eddyi} , is analogous to the DC screening current in a superconducting plate. (b) Illustration of T_{eddyi} and corresponding surface current map. (c) In the proposed passive shield, T_{eddyi} is discretized into a closed-loop coil with current i_0 . The black lines indicate cutouts on the conductor and the current flows from the red dot in the middle (P₁) to the blue dot at the bottom (arrow, P₂). The two dots are shunted by a copper bridge (not shown) to close the loop and cancel the turn-to-turn radial current.

the applied field, can be written as follows:

$$CT + Du = -i\omega B_{app}, \quad (5)$$

where

$$C \equiv -\sigma_s^{-1} \nabla^2 + i\omega K^* \quad (6)$$

is the impedance operator and

$$D \equiv -i\omega B_0 \frac{\partial}{\partial z} \quad (7)$$

is the motional EMF operator. In Eq. (6), the symbol K^* indicates convolution with a dipolar field kernel, which converts surface dipole density (T) into a normal magnetic field on the surface. The two terms of the operator C correspond to the resistance operator \mathcal{R} and $i\omega$ times self-inductance operator \mathcal{L} , which can be defined as

$$\mathcal{R} \equiv -\sigma_s^{-1} \nabla^2, \quad (8)$$

$$\mathcal{L} \equiv K^*. \quad (9)$$

Such designation can be justified from the energy dissipation and self-inductance expressions of a stream function shown in

Ref. 18 (also see Sec. II B 2). Being related to measurable, positive quantities, both \mathcal{R} and \mathcal{L} are positive definite.

1. General properties of the coupled equations

Equations (1) and (5) constitute inhomogeneous coupled equations for u and T , with a source term being proportional to B_{app} . Both u and T , therefore, scale linearly with B_{app} . The two operators that are responsible for magneto-mechanical coupling, \mathcal{B} and \mathcal{D} , are both proportional to the static field B_0 . In the absence of B_0 , u and T are decoupled. The frequency dependence appears in the mechanical force operator (\mathcal{A}) for damping and inertia, as well as in \mathcal{C} and \mathcal{D} for self- and motion-induced EMF. If the conductor thickness is larger than the skin depth $\delta(\omega) = 1/\sqrt{\pi\mu_0\sigma f}$, the effective surface conductivity becomes frequency dependent: $\sigma_s = \sigma_s(\omega) \approx \sigma\delta(\omega)$. Finally, if mechanical damping is ignored in Eq. (3), \mathcal{A} is real and no phase shift is involved in the equation of motion [Eq. (1)]. This compares with Eq. (5) where all operators are imaginary except for \mathcal{R} in \mathcal{C} . The two terms that single out, namely mechanical damping and electrical resistance, are associated with energy dissipation.

2. Magnetic damping and stiffening

Magnetic damping and stiffening refer to apparent increase in mechanical damping and stiffness of a conductive object when driven mechanically in the presence of a static magnetic field.

While this is not the main topic of this paper, our coupled equations naturally predict the existence of such phenomena. Since the analysis lends support to the validity of our equations, the discussion of magnetic damping/stiffening is presented in [Appendix B](#).

3. Motional impedance

The circuit equation analog of magnetic damping/stiffening is motional impedance (resistance/inductance). This is obtained by the following formal solution of the coupled equations for T . We solve Eq. (1) for u and substitute this into Eq. (5) to eliminate u . The result is

$$T = (\mathcal{C} + \mathcal{D}\mathcal{A}^{-1}\mathcal{B})^{-1}(-i\omega B_{app}). \quad (10)$$

The magneto-mechanical term $\mathcal{D}\mathcal{A}^{-1}\mathcal{B}$ is proportional to B_0^2 . We observe that to the extent \mathcal{C} represents the impedance of T , the effect of B_0 is to add $\mathcal{D}\mathcal{A}^{-1}\mathcal{B}$ to the impedance. We will, therefore, call this a motional impedance operator \mathcal{Z}_M :

$$\mathcal{D}\mathcal{A}^{-1}\mathcal{B} = \mathcal{Z}_M, \quad (11)$$

$$\begin{aligned} \mathcal{Z}_M &\equiv -i\omega B_0 \frac{\partial}{\partial z} (-\mathcal{F}_M - \rho_m \omega^2)^{-1} \left(B_0 \frac{\partial}{\partial z} \right) \\ &= -i\omega B_0^2 \frac{\partial}{\partial z} (-\mathcal{F}_M - \rho_m \omega^2)^{-1} \frac{\partial}{\partial z}. \end{aligned} \quad (12)$$

This expression, while being formal, can give us considerable insight into the phenomenon of magneto-mechanical resonance. Let us call the (i times) imaginary part of \mathcal{Z}_M as $i\omega\mathcal{L}_M$, where \mathcal{L}_M is motional inductance, a real operator. The operator $i\omega\mathcal{L}_M$ adds to the (i times) inductive part of \mathcal{C} , which is $i\omega K^*$. As shown in the following subsection, while the conventional inductance operator K^* is positive definite, \mathcal{L}_M is not, and its sign (of the eigenvalues) generally depends on ω . It is then possible that the motion-altered inductance of the plate ($K^* + \mathcal{L}_M$) ceases to be positive and undergoes zero crossing at a certain frequency for certain current eigenmodes. This is analogous to the cancelation of inductive impedance by a capacitor in an LC circuit. We can, therefore, call this phenomenon magneto-mechanical resonance. At the resonance, the total eddy current in the conductive plate inside a static field can be much larger than at zero field. Below, we will examine this more closely using plane wave eigenmodes of an infinitely large plate.

4. Special case: magneto-mechanical resonance of an infinite plate

Using Eqs. (8), (9), and (11), we rewrite Eq. (10) as

$$T = (\mathcal{R} + i\omega\mathcal{L} + \mathcal{Z}_M)^{-1}(-i\omega B_{app}). \quad (13)$$

In a special case where the plate is infinitely large, the operators \mathcal{R} , \mathcal{L} , and \mathcal{Z}_M are simultaneously diagonalized by the plane wave eigenfunctions labeled by the wavevector $\vec{k} = (k_z, k_x)$. The corresponding eigenvalues are

$$\mathcal{R}: -\sigma_s^{-1}\nabla^2 = \sigma_s^{-1}k^2 \geq 0, \quad (14)$$

$$\mathcal{L}: K^* = \frac{\mu_0}{2} k \geq 0, \quad (15)$$

$$\mathcal{Z}_M: i\omega B_0^2 \frac{\partial}{\partial z} (-D\nabla^4 - i\omega\lambda + \rho_m\omega^2)^{-1} \frac{\partial}{\partial z} = \frac{i\omega B_0^2 k_z^2}{Dk^4 - \rho_m\omega^2 + i\omega\lambda}. \quad (16)$$

See [Appendix A](#) for Eq. (15). We used Eq. (3) for \mathcal{F}_M in Eq. (16). At mechanical resonance where $Dk^4 = \rho_m\omega^2$, Eq. (16) avoids singularity by the damping term $i\omega\lambda$ in the denominator. This situation is similar to the mechanical resonance of a damped, simple harmonic oscillator.

Combining Eqs. (13)–(16), we can write T in the spatial Fourier domain as

$$T(\vec{k}) = \frac{-i\omega}{\sigma_s^{-1}k^2 + i\omega\left(\frac{\mu_0}{2}k + \frac{B_0^2 k_z^2}{Dk^4 - \rho_m\omega^2 + i\omega\lambda}\right)} B_{app}(\vec{k}) \quad (\text{Infinite plate}), \quad (17)$$

where all independent variables are real.

As we increase ω from zero, we observe that for each spatial mode \vec{k} , we encounter two resonances. First is the mechanical resonance where the real part of the denominator of \mathcal{Z}_M vanishes, at $Dk^4 = \rho_m\omega^2$. This is the frequency, to be called ω_{mech} , at which the plate would undergo the maximum displacement in response to pure mechanical excitation, absent Lorentz force. The second, magneto-mechanical resonance occurs when the real part of \mathcal{Z}_M becomes negative and cancels the conventional inductance $(\mu_0/2)k$. It can happen when $Dk^4 < \rho_m\omega^2$, that is, past the mechanical resonance ($\omega > \omega_{mech}$) where the motion and force are out of phase. The importance of mechanical phase reversal in the context of magneto-mechanical resonance is illustrated in [Fig. 3](#).

Below, we summarize a few properties of magneto-mechanical resonance of an infinite conducting plate.

- (i) The magneto-mechanical resonance frequency ω_{mm} satisfies $\omega_{mm} > \omega_{mech}$.
- (ii) ω_{mm} is a function of wavevector \vec{k} .
- (iii) At the resonance, the reactive (inductive) part of the total impedance of the current mode vanishes.
- (iv) If the zero-field impedance of the mode is dominated by the reactive term (i.e., $\mu_0\omega k/2 \gg \sigma_s^{-1}k^2$), magneto-mechanical resonance at non-zero static field can greatly increase the eddy current response T/B_{app} by nulling such a term. Because of frequency dependence in other terms of Eq. (17), the exact maximum of $|T/B_{app}|$ may not occur at $\omega = \omega_{mm}$.

5. Relationship with eddy image current

From the definition of \mathcal{Z}_M (Eq. 12), it can be recognized that as $\omega \rightarrow \infty$, $\mathcal{Z}_M \rightarrow 0$, and Eq. (13) becomes

$$\lim_{\omega \rightarrow \infty} T = \lim_{\omega \rightarrow \infty} (\mathcal{R} + i\omega\mathcal{L})^{-1}(-i\omega B_{app}) = -\mathcal{L}^{-1}B_{app}. \quad (18)$$

This is the stream function of the eddy image current,

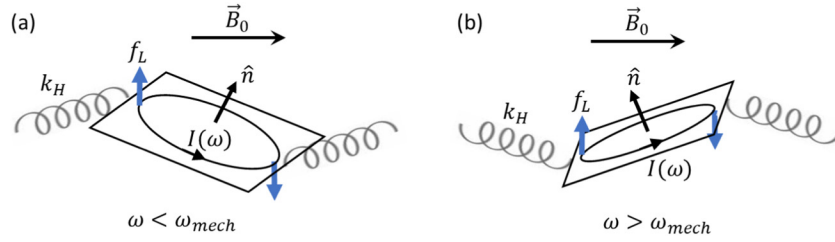


FIG. 3. Illustration of motional inductance and onset of magneto-mechanical resonance. (a) At low frequencies ($\omega \ll \omega_{mech}$), the Lorentz force f_L acting on an oscillating current $I(\omega)$ tilts the plate towards and away from \vec{B}_0 in phase with the current. When the current is positive, the tilt of the normal vector \hat{n} is toward \vec{B}_0 . Such tilt results in positive (locally upward) flux of \vec{B}_0 threading the loop, making motional inductance positive. (b) At high frequencies ($\omega \gg \omega_{mech}$), the Lorentz force and angular tilt of \hat{n} are 180° out of phase; when the current is positive, the tilt is still away from \vec{B}_0 trying to catch up. In this case, \vec{B}_0 threads the current in the negative direction, or locally downwards, and the motional inductance is negative. If the negative motional inductance cancels the positive self-inductance, the loop is at magneto-mechanical resonance. Then, the current induced by an applied oscillating magnetic field (not shown) is impeded only by the resistance of the loop. k_H denotes the spring constant.

previously called T_{eddyi} . That is,

$$B_{app} = -\mathcal{L}T_{eddyi}. \quad (19)$$

Physically, this means that at high enough frequencies where mechanical motion cannot keep up with the electromagnetic drive, and when inductive impedance dominates resistance, the induced eddy current completely nulls the applied normal magnetic field. We can now express T in terms of T_{eddyi} in Eq. (13),

$$T = (\mathcal{R} + i\omega\mathcal{L} + \mathcal{Z}_M)^{-1}(i\omega\mathcal{L}) T_{eddyi}, \quad (20)$$

while Eq. (17), for an infinite plate, becomes

$$T(\vec{k}) = \frac{i\omega(\mu_0/2)k}{\sigma_s^{-1}k^2 + i\omega\left(\frac{\mu_0}{2}k + \frac{B_0^2 k_z^2}{Dk^4 - \rho_m\omega^2 + i\omega\lambda}\right)} T_{eddyi}(\vec{k}). \quad (\text{Infinite plate}) \quad (21)$$

Equation (21) shows that, at each frequency and wavevector, the mode amplitude of the shield current differs from an ideal eddy current by a multiplicative factor. The magnitude of this factor can be much larger than unity near $\omega = \omega_{mm}$.

B. Magneto-mechanical coupled equations for a shield plate patterned into an eddy image loop

Let us assume that we freeze the eddy image current T_{eddyi} in space [Fig. 2(b)] and discretize it by cutting lines along its contours: $\{T_{eddyi} = c_n\}$ where c_n ($n = 1, 2, \dots$) is a set of currents that divide T_{eddyi} into $N_{turns} \gg 1$ equidistant levels [Fig. 2(c)]. Following the standard practice of surface coil design,¹⁹ we assume that adjacent contours are connected in series and a return path is provided from the last to the first contour so that all the contour lines are traversed in one stroke between the input (P_1) and output (P_2) terminals. If we now apply a current i_0 from P_1 to P_2 that corresponds to the contour spacing, $i_0 = c_2 - c_1$, such current will approximate the continuous surface current defined by T_{eddyi} . The patterned passive shield proposed in this work consists of a closed loop formed by short-circuiting P_1 and P_2 . When acted on by a time-

dependent magnetic field from a driving coil, an induced current $I(t)$ in the loop will tend to shield the space opposite to the driving coil from such magnetic field. The goal of this section is to calculate $I(t)$ in the presence of magneto-mechanical coupling.

1. Current and motional degrees of freedom of the patterned conductor

Let us define a dimensionless static function,

$$\tilde{T}_{eddyi}(z, x) \equiv T_{eddyi}(z, x)/i_0. \quad (22)$$

This can be viewed as a continuous (smoothed) version of the “number-of-turns” function $N(z, x)$ of the discretized surface current described above. $N(z, x)$ is defined by counting (integrating) the number of contour lines (turns) in a direction-sensitive way; that is, by adding +1 if the current in the turn crosses the integration path from the left to the right, and -1 if in the other direction, as one moves from the edge of the plate to the point (z, x) . If the patterned passive shield carries a current $I(t)$ (or $I(\omega)$ in the frequency domain), the corresponding stream function is

$$T(z, x; t \text{ or } \omega) = I(t \text{ or } \omega)N(z, x) \approx I(t \text{ or } \omega)\tilde{T}_{eddyi}(z, x). \quad (23)$$

In the limit $N_{turns} \rightarrow \infty$ and $i_0 \rightarrow 0$, $N(z, x)$ converges to \tilde{T}_{eddyi} . In what follows, we will assume such a limit (i.e., ignore discretization error) and use N and \tilde{T}_{eddyi} interchangeably.

Importantly, all the surface current degrees of freedom of the conductive plate are now condensed into a single time- or frequency-dependent variable I . Note that the magnitude of \tilde{T}_{eddyi} depends on i_0 from Eq. (22), which was somewhat arbitrarily determined during the discretization of the eddy image current. This is not a problem because the final stream function T appears as a product of I and \tilde{T}_{eddyi} , with opposite i_0 dependences.

We will assume that the surface current discretization does not affect the shield plate’s mechanical properties. This is realistic if the conductor of the shield plate is backed by a stiff, insulating substrate, which dominates the plate’s mechanical response. The motional

degrees of freedom of the patterned-shield plate still consist of the displacement field $u(z, x; \omega)$.

2. Equation of motion and circuit equation

The equation of motion for the patterned shield is obtained by substituting Eq. (23) in Eq. (1). The frequency domain equation reads

$$(-\mathcal{F}_M - \rho_m \omega^2)u = B_0 I(\omega) \frac{\partial \tilde{T}_{eddyi}}{\partial z}, \quad (24)$$

where the Lorentz force term is now time-space separated and contains a single unknown $I(\omega)$.

The circuit equation that governs I , coupled to u , is obtained from Eq. (5) by (i) replacing T with $I\tilde{T}_{eddyi}$ and (ii) multiplying the resulting equation with \tilde{T}_{eddyi} and integrating over the plane. The left- and right-hand sides of the resulting equation are, respectively,

$$\begin{aligned} lhs = & \left\{ -\sigma_s^{-1} \int \tilde{T}_{eddyi} \nabla^2 \tilde{T}_{eddyi} d^2 \vec{r} + i\omega \int \tilde{T}_{eddyi} K^* \tilde{T}_{eddyi} d^2 \vec{r} \right\} I(\omega) \\ & - i\omega B_0 \int \tilde{T}_{eddyi} \frac{\partial u}{\partial z} d^2 \vec{r}, \end{aligned} \quad (25)$$

$$rhs = -i\omega \int \tilde{T}_{eddyi} B_{app} d^2 \vec{r}. \quad (26)$$

The two integrals in the parenthesis of Eq. (25) and the integral in Eq. (26) all produce a scalar constant.

Specifically, we can identify the following: First,

$$-\sigma_s^{-1} \int \tilde{T}_{eddyi} \nabla^2 \tilde{T}_{eddyi} d^2 \vec{r} = R \quad (27)$$

is the conventional DC resistance of the loop where I flows. Second,

$$\int \tilde{T}_{eddyi} K^* \tilde{T}_{eddyi} d^2 \vec{r} = L \quad (28)$$

is the conventional self-inductance of the same loop. Finally,

$$\int \tilde{T}_{eddyi} B_{app} d^2 \vec{r} = \Phi_{app} \quad (29)$$

is the flux coupled to the loop by the applied field B_{app} . Equations (27)–(29) are further explained in Appendix C.

We can now rewrite Eqs. (25) and (26) simply as

$$RI + i\omega LI - i\omega B_0 \int \tilde{T}_{eddyi} \frac{\partial u}{\partial z} d^2 \vec{r} = -i\omega \Phi_{app}. \quad (30)$$

The third term on the left-hand side can be expressed in terms of I by eliminating u through a formal solution of Eq. (24),

$$u = -B_0 I(\omega) (\mathcal{F}_M + \rho_m \omega^2)^{-1} \frac{\partial}{\partial z} \tilde{T}_{eddyi}. \quad (31)$$

Substituting Eq. (31) to Eq. (30) yields

$$RI + i\omega LI + I \int \tilde{T}_{eddyi} \mathcal{Z}_M \tilde{T}_{eddyi} d^2 \vec{r} = -i\omega \Phi_{app}, \quad (32)$$

where \mathcal{Z}_M is the motional impedance operator, proportional to B_0^2 , defined in Eq. (12). We can now define the motional impedance parameter of the current loop \tilde{T}_{eddyi} as

$$Z_M = Z_M(\omega) \equiv \int \tilde{T}_{eddyi} \mathcal{Z}_M \tilde{T}_{eddyi} d^2 \vec{r}. \quad (33)$$

Using the imaginary part of \mathcal{Z}_M , $Im(\mathcal{Z}_M) = \omega \mathcal{L}_M$, we also define the motional inductance of the loop as

$$L_M = L_M(\omega) \equiv \int \tilde{T}_{eddyi} \mathcal{L}_M \tilde{T}_{eddyi} d^2 \vec{r}. \quad (34)$$

This signifies the flux per 1 A in the loop that is caused by its physical displacement in the B_0 field. The final solution for the current in the presence of magneto-mechanical coupling is, from Eqs. (32) and (33),

$$I = I(\omega) = \frac{-i\omega \Phi_{app}}{R + i\omega L + Z_M(\omega)}. \quad (35)$$

Magneto-mechanical resonance occurs when the imaginary (reactive) part of $Z_M(\omega)$ becomes negative and cancels the self-inductance L . The precise line shape of $I(\omega)$ depends on the functional form of $Z_M(\omega)$, which is hard to reduce analytically in a non-infinite plate. On the other hand, $I(\omega)$ can be determined experimentally from the measured impedance of the loop, $Z(\omega) \equiv R + i\omega L + Z_M(\omega)$. To measure Z , one should break the short between the terminals P_1 and P_2 and probe their voltage difference while applying sinusoidal current at different ω . Such measurement can be used to characterize a patterned shield regarding its magneto-mechanical behavior.

3. Relationship with eddy image current

In the high-frequency limit, motional impedance vanishes and Eq. (35) converges to $\lim_{\omega \rightarrow \infty} I(\omega) = -\Phi_{app}/L$. This limiting current equals the ideal eddy image current in the patterned shield, which was previously defined as i_0 . That is,

$$\lim_{\omega \rightarrow \infty} I(\omega) = -\frac{\Phi_{app}}{L} = i_0. \quad (36)$$

This relation can be used to eliminate Φ_{app} in Eq. (35),

$$I(\omega) = \frac{i\omega L}{R + i\omega L + Z_M(\omega)} i_0. \quad (37)$$

Multiplying both sides with \tilde{T}_{eddyi} , we obtain the patterned-shield's current in terms of its stream function,

$$T(z, x; \omega) = I(\omega) \tilde{T}_{eddyi}(z, x) = \frac{i\omega L}{R + i\omega L + Z_M(\omega)} T_{eddyi}(z, x). \quad (38)$$

This highlights the fact that for a patterned shield, the eddy current solution has the same spatial shape (by design) as the ideal eddy current but with an ω -dependent scale factor. We note that

for a given applied field B_{app} , as N_{turns} changes all the expectation values R , L , Z_M scale as N_{turns}^2 , the number-of-turns function $N(z, x)$ and \tilde{T}_{eddyi} are proportional to N_{turns} , and I and i_0 are inversely proportional to N_{turns} .

C. Comparison between continuous and patterned passive shields

It is interesting to compare the surface current solutions for continuous [Eq. (20)] and patterned [Eq. (38)] shields. In the latter, T is a scaled version of the eddy image current, where the proportionality constant corresponds to the operator fraction in Eq. (20) after all operators are replaced by their expectation values with respect to the turns-number function \tilde{T}_{eddyi} . The expectation value of an operator \mathcal{O} with respect to a function $f(\vec{r})$ is defined as,²⁰

$$\langle \mathcal{O} \rangle = \langle f | \mathcal{O} | f \rangle \equiv \int f^*(\vec{r}) \mathcal{O} f(\vec{r}) d^2\vec{r}. \quad (39)$$

R , L , Z_M , and L_M in Eqs. (27), (28), (33), and (34) as well as Z defined after Eq. (35) correspond to the expectation values of the operators \mathcal{R} , \mathcal{L} , \mathcal{Z}_M [Eqs. (8), (9), and (12)], and \mathcal{L}_M [after Eq. (12)], and \mathcal{Z} , respectively. Here, we define the total impedance operator $\mathcal{Z} \equiv \mathcal{R} + i\omega\mathcal{L} + \mathcal{Z}_M$.

Further insights can be gained if we consider the expansion of the stream functions in terms of the eigenfunctions of \mathcal{Z} ,

$$|j\rangle = f_j(z, x), \quad (j = 1, 2, \dots) \quad (40)$$

that satisfy

$$\mathcal{Z}|j\rangle = \zeta_j|j\rangle, \quad (41)$$

where ζ_j are the eigenvalues. (Index j should not be confused with the surface current.) Now, consider the following expansion of the eddy image current:

$$T_{eddyi} = \sum_j a_j |j\rangle. \quad (42)$$

In general, both a_j and $|j\rangle$ are complex. We want to express the stream function solutions for the continuous and patterned passive shields using the same expansion.

First, the continuous shield solution can be written, from Eq. (20), as

$$T(\text{continuous}) = \mathcal{Z}^{-1}(i\omega\mathcal{L})T_{eddyi} = i\omega \sum_j \mathcal{Z}^{-1}|j\rangle \langle j | \mathcal{L} T_{eddyi} = i\omega \sum_j \frac{\langle j | \mathcal{L} | T_{eddyi} \rangle}{\zeta_j} |j\rangle, \quad (43)$$

where we used the bra-ket notation for the eddy image. Equation (43) states that each current mode of T_{eddyi} is multiplied by a factor proportional to $1/\zeta_j$. Recall that \mathcal{Z} and, therefore, its eigenvalues ζ_j are ω -dependent. Equation (43) implies that if any of the ζ_j values (nearly) vanishes at mode-specific magneto-mechanical resonance, the entire solution T undergoes a resonant peak. This partly explains the complexity of magneto-mechanical resonance spectra often encountered in conductive shells and plates.³

This situation is contrasted with that of a patterned shield. From Eq. (38), we see that

$$T(\text{patterned}) = \frac{i\omega\langle \mathcal{L} \rangle}{\langle \mathcal{Z} \rangle} T_{eddyi}. \quad (44)$$

Using expansion equation (42) to rewrite the denominator, we get

$$T(\text{patterned}) = i\omega \frac{\langle T_{eddyi} | \mathcal{L} | T_{eddyi} \rangle}{\sum_j \zeta_j |a_j|^2} \sum_j a_j |j\rangle. \quad (45)$$

Here, the singularity of individual modes ($\zeta_j = 0$) does not directly translate into the singularity of T since the denominator is a *weighted sum of all mode eigenvalues*. Zero crossing of such a sum generally occurs much less frequently than those of individual ζ_j in aggregate. This can be understood from the fact that if individual

ζ_j 's are an n th order polynomial (of ω), their weighted sum is still an n th order polynomial, permitting at most n zero crossings. One can expect, therefore, that the patterned passive shield will exhibit fewer resonance peaks than the continuous shield. Simpler resonance spectra in a patterned shield were indeed observed in our experiments described below.

III. EXPERIMENTAL METHODS

A. Leakage field frequency response function

Figure 4 shows the experimental setup. Gradient leakage field was modeled by the magnetic field generated by a 20 cm-diameter, 10-turn circular loop coil ("driving coil") wound from a 1 mm-diameter magnet wire. The field was sensed by a 5 cm-diameter solenoidal pickup coil ("sensing coil"), which was mounted on a wooden stick that could be translated horizontally (z direction) above the driving coil. The center-to-center vertical (y direction) distance between the pickup coil and the driving coil was 9.6 cm. The voltage at the pickup coil provided a measure of frequency-weighted magnetic field according to

$$V_{pickup} = -i\omega A_{eff} B_{pickup}, \quad (46)$$

where A_{eff} is the effective area of the pickup coil. The effective area was not measured independently and was left as a common, real-valued scale factor throughout the experiment. This was

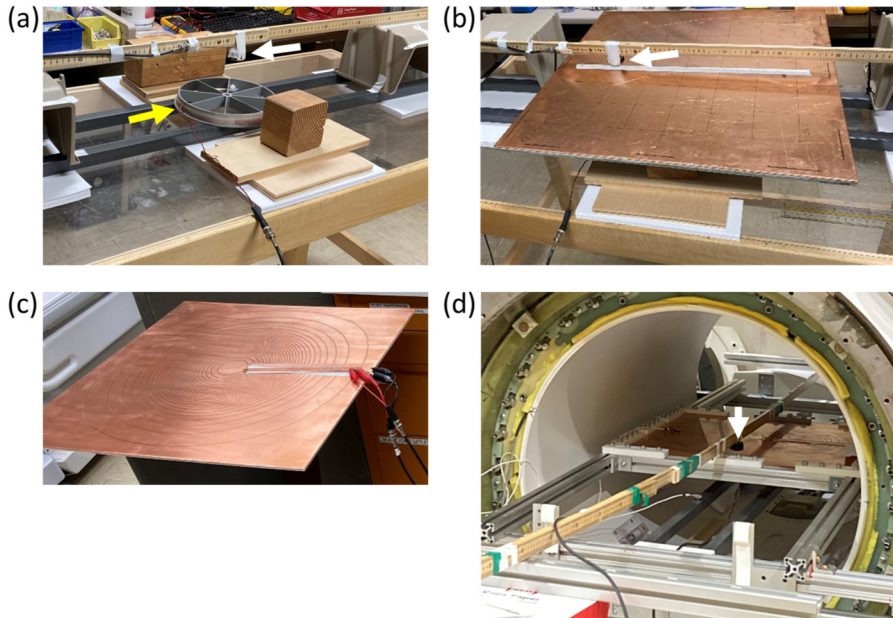


FIG. 4. Experimental setup. (a) Driving (yellow arrow) and sensing (white arrow) coils. (b) Solid copper plate placed between the driving (hidden below the plate) and sensing (white arrow) coils. (c) Patterned copper during impedance measurement. The two ends of the spiral pattern were shorted during the FRF measurements. (d) Setup in a whole-body 3 T magnet with sensing coil indicated by the white arrow. The copper plate was mounted on an aluminum frame fixed against the magnet end flanges, while the sensing coil was hanging from a wooden pole supported from the floor of the room.

permissible as our interest was in relative changes in the leakage field under different shielding configurations.

The experiment consisted of measuring the frequency response function (FRF), defined as the ratio between V_{pickup} and the driving coil current in the frequency domain, in the following four configurations: (i) First, the FRF was measured at nineteen z locations ($z = -9\Delta z$ to $+9\Delta z$, with $\Delta z = 2.54$ cm) with no conductive barrier between the two coils; (ii) second, a 1.6 mm-thick solid copper plate backed by a 9.6 mm-thick fiberglass plate, both measuring 55.9×55.9 cm² in the plane, was inserted between the coils [Fig. 4(b)]. The distance between the center of the driving coil and the top surface of the copper plate was 8.1 cm. (iii) Third, the setup (with copper) was moved inside the bore of a 3 T whole-body MRI magnet. (iv) Finally, the solid copper plate was replaced by a copper plate with a spiral pattern machined according to the simulated eddy current image of the driving coil [Figs. 4(c) and 4(d)]. The spiral pattern was bridged by a copper strip to make a single closed loop that allowed current to flow in a way to mimic the eddy image.

In order to minimize the mechanical transmission of vibration between the driving coil and the copper plates, the horizontal plastic rods that held the driving coil [Fig. 4(a)] were mounted on aluminum crossbars at both end flanges of the magnet via a 4 mm-thick, soft foam-backed double sticky tape (similar to part #7626A274, McMaster-Carr, Elmhurst, IL, USA). Accelerometer measurements confirmed that this mounting was more effective in vibration isolation than conventional bolt mounting with rubber paddings.

The eddy image pattern was calculated based on the dimensions of the driving coil and the coil-shield distance in COMSOL (COMSOL Multiphysics, Burlington, MA, USA) and discretized in MATLAB (MathWorks, Natick, MA, USA) into a spiral pattern with $N_{\text{turns}} = 25$. The pattern was machined on a 1.6 mm-thick copper blank plate with 1 mm cut width. A 9.6 mm-thick fiberglass plate

backed the copper. The narrowest conductor path was 4.4 mm wide. N_{turns} was decided considering the trade-off between the fidelity of stream function representation (which favors large N_{turns}) and mechanical integrity and manufacturability (favoring less turns).

All FRF measurements were carried out with LMS SCADAS Mobile (Siemens PLM Software, Plano, TX, USA) multi-channel data acquisition system (software module: Spectral Testing 11B) with integrated signal generator. A pseudo-white noise voltage signal with 10 kHz bandwidth and 3.125 Hz resolution was fed into an audio amplifier (Crown Audio, Los Angeles, CA, USA), and its output was applied to the driving coil via a 0.1Ω current-sensing resistor. The pickup coil voltage and the voltage of the resistor were recorded by the data acquisition system, and FRF was computed real-time.

B. Impedance spectrum and prediction of FRF

The complex impedance spectrum $Z(\omega)$ of the spiral pattern was measured in the fourth configuration above, with the copper strip electrically open. A dynamic signal analyzer (35670A, Keysight, Santa Rosa, CA, USA) measured the impedance in the frequency range $5 \text{ Hz} \leq f \leq 10005 \text{ Hz}$ at 1601 logarithmically sampled frequency points. The data were processed in MATLAB to calculate the theoretical leakage field spectrum of the patterned-copper shield as explained below.

The magnetic field at a given pickup coil location B_{pickup} consists of two parts: magnetic field from the driving coil current $I_{\text{dr}}(\omega)$ and that of the shield current $I_{\text{sh}}(\omega)$. That is,

$$B_{\text{pickup}}(z, x; \omega) = b_{\text{dr}}(z, x)I_{\text{dr}}(\omega) + b_{\text{sh}}(z, x)I_{\text{sh}}(\omega), \quad (47)$$

where the static functions b_{dr} and b_{sh} denote magnetic fields for unit current in the driving coil and the shield pattern, respectively.

At high frequencies, B_{pickup} approaches zero by the design of the patterned shield,

$$\lim_{\omega \rightarrow \infty} (b_{dr}I_{dr} + b_{sh}I_{sh}) = 0. \tag{48}$$

We can, therefore, rewrite Eq. (46) as

$$\begin{aligned} V_{pickup}(\omega) &= -i\omega A_{eff} b_{sh} I_{dr}(\omega) \left(\frac{I_{sh}(\omega)}{I_{dr}(\omega)} + \frac{b_{dr}}{b_{sh}} \right) \\ &= -i\omega A_{eff} b_{sh} I_{dr}(\omega) \left(\frac{I_{sh}(\omega)}{I_{dr}(\omega)} - \lim_{\omega \rightarrow \infty} \frac{I_{sh}(\omega)}{I_{dr}(\omega)} \right), \end{aligned} \tag{49}$$

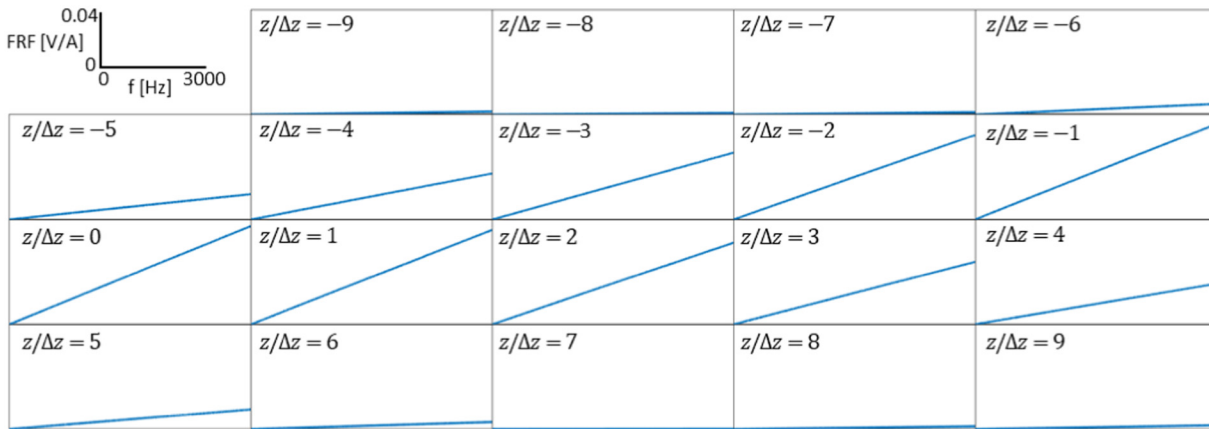
where the last equality comes from Eq. (48).

Note that the FRF experiment measures the ratio $V_{pickup}(\omega)/I_{dr}(\omega)$. In Eq. (49), the most non-trivial term is I_{sh}/I_{dr} , the shield current normalized by the driving current. This term is proportional to $I(\omega)/\Phi_{app}$ calculated in Eq. (35) and can be estimated by replacing the denominator of the right-hand side of Eq. (35) with the measured impedance $Z(\omega)$. Combining this with Eq. (49), we obtain

$$FRF \equiv \frac{V_{pickup}(\omega)}{I_{dr}(\omega)} = (\text{real constant}) \times \omega \times \left(\frac{\omega}{Z(\omega)} - \lim_{\omega \rightarrow \infty} \frac{\omega}{Z(\omega)} \right). \tag{50}$$

The last (limit) term can be estimated from the high-frequency asymptote of the measured $Z(\omega)$.

(a) Unshielded, outside magnet



(b) Solid copper shield, outside magnet

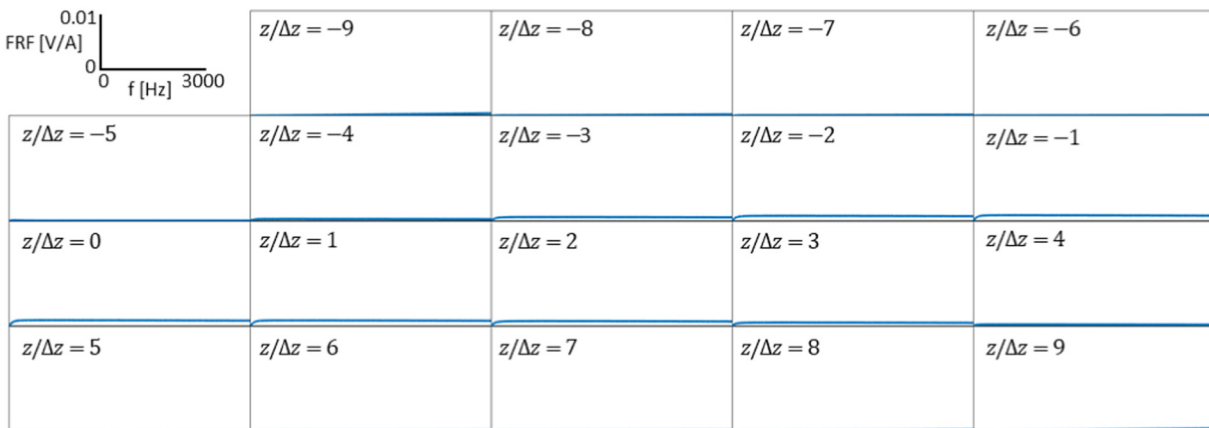


FIG. 5. Frequency response functions for unshielded baseline setup (a) and setup with solid copper plate between the driving and sensing coils (b) outside the magnet. Each box contains a current-to-voltage FRF spectrum on the axis defined at the top left corner. Nineteen FRFs obtained at different z locations of the sensing coil are presented. Note fourfold larger vertical scale in (a). Solid copper outside the magnet provides nearly perfect shielding.

IV. RESULTS

A. Frequency response function of the leakage field

Figure 5 shows the measured FRF at frequencies up to 3 kHz in the first two configurations (with and without copper plate outside the magnet). The unshielded FRF [Fig. 5(a)] is linear in frequency as expected from Eq. (46). This simply means that there is no frequency-dependent magnetic field in the system without a metallic shield in place. The z -dependence originates from the static (Biot-Savart law) magnetic field profile of the driving coil. Figure 5(b) demonstrates near complete shielding of the driving field by solid copper. Note that the vertical scale is magnified fourfold in Fig. 5(b).

Figure 6 shows the measured FRF at 3 T with solid and patterned passive copper shields. Comparing Fig. 6(a) with Fig. 5(b), we find dramatic degradation of shielding performance as the copper plate is placed inside a strong static field. This is manifested by many leakage field peaks in the FRF of Fig. 6(a), which are caused by magneto-mechanical interaction. Importantly, the FRF spectral shapes are different at different z positions, which indicates multiple surface current modes involved. As expected, the magneto-mechanical response peaks subside in the high-frequency limit, above about 2 kHz.

Figure 6(b) contains the main result of the experimental part of this study. It shows that the patterning of the copper passive

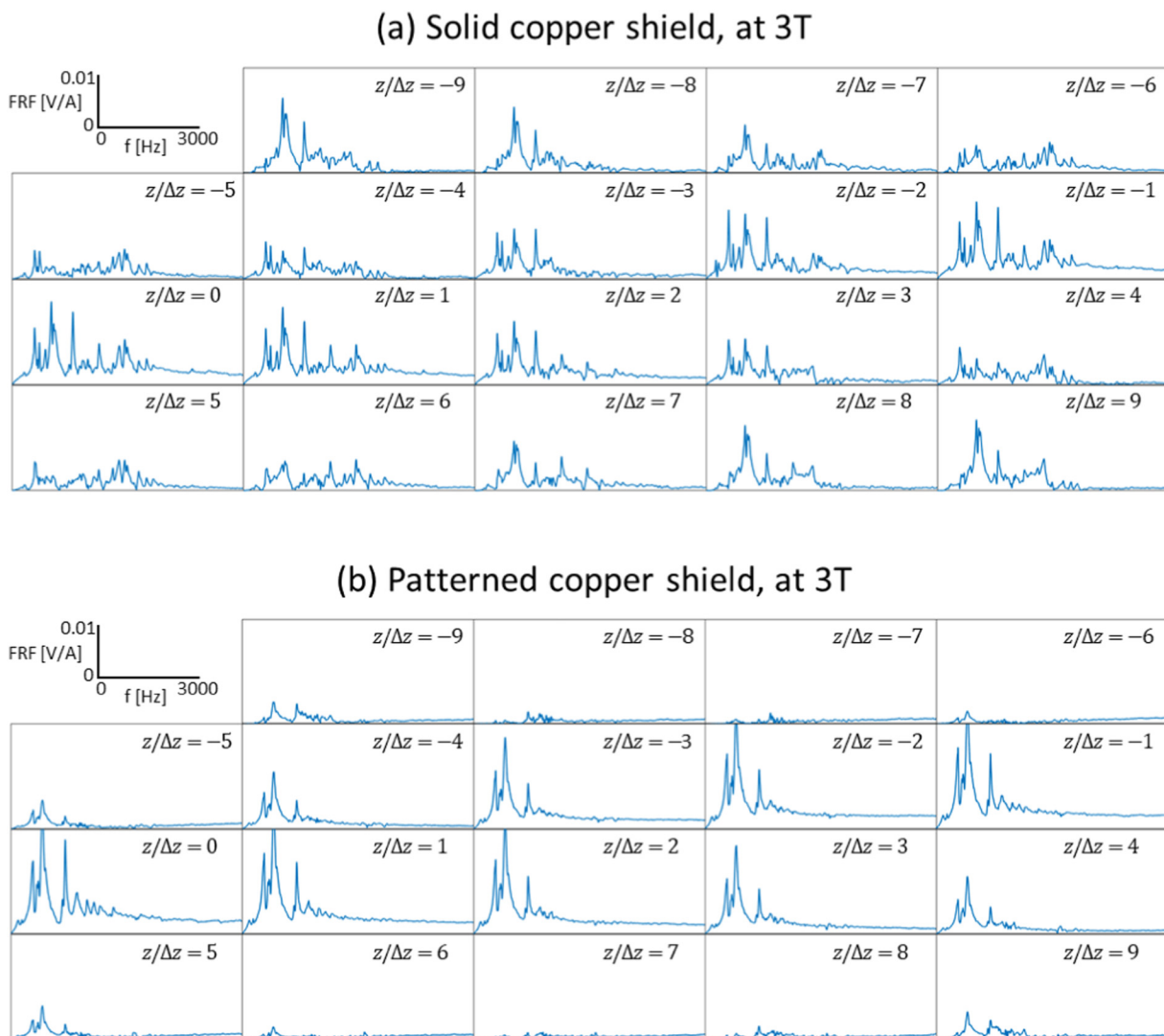


FIG. 6. Frequency response functions for solid (a) and patterned (b) copper shields inside a 3 T magnet. Compared to Fig. 5(b), shielding is severely disrupted at 3 T with numerous magneto-mechanical resonance peaks appearing as a result of motional eddy current. Patterned shield makes the leakage field peaks more localized in space and frequency than solid copper.

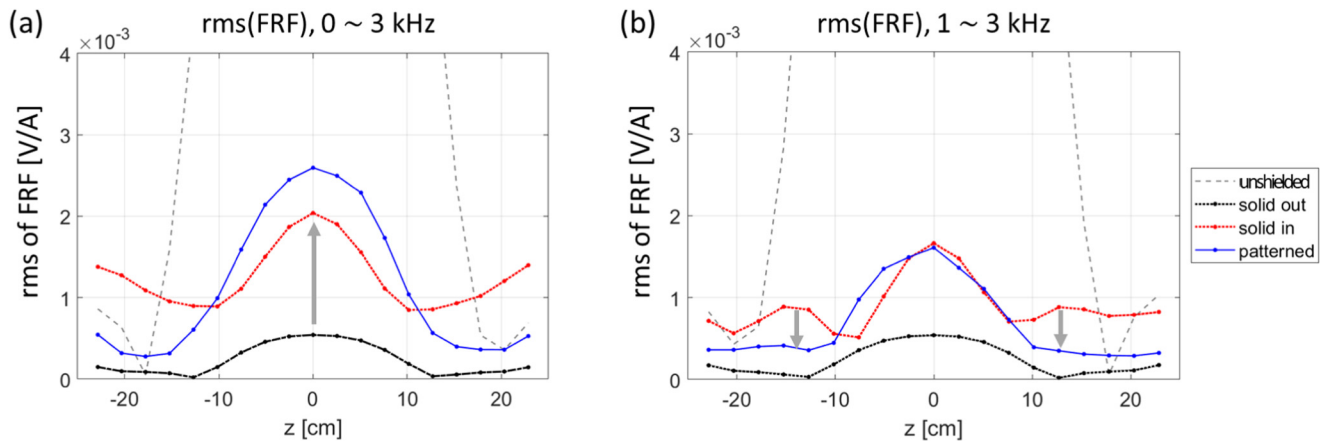


FIG. 7. Root-mean-square of the measured pickup-coil FRF over 0–3 (a) and 1–3 kHz (b) as a function of z . Large difference between solid copper shields in (red) and out of (black) the magnet highlights leakage field amplification [arrow in (a)] due to motional eddy current. Patterned-copper shield in the magnet (blue) makes the leakage field more concentrated in frequency and space [arrows in (b)] compared to solid copper.

shield drastically changes the spatial and spectral profile of the magnetic field that goes through the shield. In particular, the patterned shield shows substantially reduced leakage field magnitudes in peripheral regions ($|z/\Delta z| > 4$) and at high frequencies ($f > 1$ kHz). Although the leakage field was higher near $z = 0$ and $f < 1$ kHz, Fig. 6 reveals that the patterned-copper FRF is more localized in space and frequency, and exhibits more consistent spectral shapes across z . This reflects the fact that the leakage field primarily originates from a single current mode defined by the pattern. Slight changes in the spectral patterns near the edge ($|z/\Delta z| > 7$) of the plate are likely caused by localized eddy current in the relatively wide copper traces in the peripheral regions. The spectral and spatial localization of the leakage field can also be

appreciated in Fig. 7, where the root-mean-square (RMS) of FRF as a function of z is plotted for different frequency bands. The RMS leakage field greatly increased as the solid copper shield moved into the 3 T magnet [black vs red curves in Figs. 7(a) and 7(b)], which was then significantly reduced at peripheral z positions ($|z| > 10$ cm) by patterning (blue curves). At high frequencies [1–3 kHz, Fig. 7(b)], patterning reduced or held constant the RMS FRF at most z locations [Fig. 7(b)].

B. Impedance spectrum vs FRF

The spectral shape of the patterned-shield leakage field could be well predicted from the impedance measurement as shown in Fig. 8.

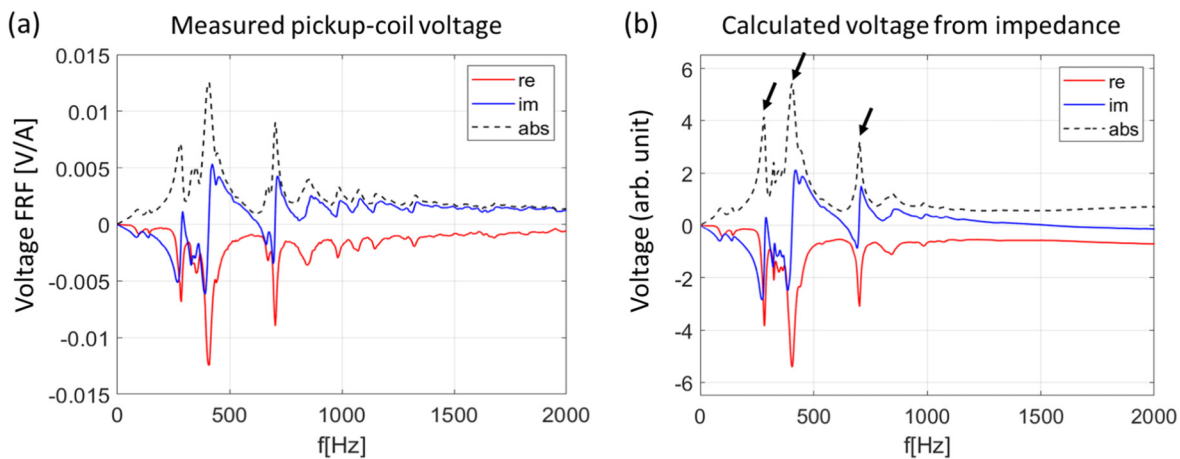


FIG. 8. Measured (a) and calculated (b) pickup coil voltage FRF spectra for the patterned-copper shield. Measurement was taken with the sensing loop at $z = 0$. Calculation is based on the impedance of the copper spiral pattern open-circuited and measured in the magnet. Major motional eddy current peaks are well reproduced in the calculated spectrum [arrows in (b)].

The real and imaginary parts of the leakage field FRF in Fig. 6(b), at $z = 0$, are reproduced in Fig. 8(a). All major magneto-mechanical resonance peaks observed in the data are well reproduced in the spectrum shown in Fig. 8(b), which was calculated from the measured complex impedance spectrum. This validates (i) that the observed leakage field profiles in Fig. 6(b) are indeed produced by the current in the cut-out pattern and (ii) that for the patterned loop shield, the magneto-mechanical resonance spectrum can be accurately predicted by impedance measurement of the loop at the same static field. The latter fact significantly simplifies the test of a patterned passive shield as impedance can be easily measured at the terminals of the loop without setting up inductive driving and sensing coils around the shield.

V. SUMMARY AND DISCUSSION

In this work, we developed and analyzed magneto-mechanical coupled equations for a conductive plate in a static magnetic field. We found that coupling between motional and electrical degrees of freedom originates from the Lorentz force acting on moving charges. In the coordinate system chosen, such force is responsible for both the vertical (y -directional) mechanical force acting on x -directional current and the x -directional electromotive force acting on the vertically vibrating conductor. These effects manifest themselves as magnetic damping and stiffening in the mechanical response of the plate, and motional inductance and impedance in its electrical response. Our equations showed that, interestingly, magnetic damping is caused by electrical resistance, and the real part of the motional impedance comes from mechanical damping. This is reasonable based on energy conservation; if there is extra damping when an object undergoes forced motion, the dissipated energy has to go somewhere, such as electrical resistive heating. All response coefficients (such as impedance and damping coefficient) that result from magneto-mechanical coupling are proportional to B_0^2 .

It is interesting and non-trivial that magnetic stiffening is always positive while motional inductance can take both signs. We found that a negative motional inductance can act as a pseudo-capacitance to cancel the electrical inductance of a current mode, leading to the resonant amplification of the electrical response of the system. In the case of an infinitely large plate, we found that such magneto-mechanical resonance occurs past a mechanical resonance frequency where the system's mechanical response undergoes phase reversal. We conjecture that similar behavior will be observed for finite-sized plates as long as the plate's dimensions are larger than the length scales of the relevant current modes.

While our analysis was strictly based on a flat conductive plate, it is plausible to expect that most qualitative conclusions and insights gained will continue to hold in other geometries, such as a cylindrical one, which is most relevant in common MRI scanners. This is because the derivation of the main coupled equations detailed in Appendix A was drawn from general principles of Newton's and Maxwell's equations, and did not rely in a fundamental way on geometry-specific features and properties. In addition, qualitative observations such as quadratic dependence of magnetic damping on B_0 and magneto-mechanical resonance agree with previous, anecdotal reports and analyses based on simpler

systems and equations.^{16,21,22} To our knowledge, our work is the first to formulate the magneto-mechanical coupling problem on a distributed current as opposed to a lumped-element circuit. Extending the present work to a cylindrical passive shield as well as a finite-sized plate with realistic boundary conditions is left for future investigation.

From Fig. 6, we find that the patterned shield provides shielding efficiency comparable to the continuous conductive plate in the high-frequency limit past magneto-mechanical resonances (above ~ 2 kHz). This validates the idea that high-frequency shielding is provided by one specific current mode, namely, the eddy image current, and, therefore, cutting such a pattern into the continuous plate preserves the plate's shielding capability above certain frequency thresholds.

The main idea of the proposed method is to preserve the desired, shielding eddy current while minimizing vibration-induced eddy currents in the presence of a strong static field. This strategy is most effective when the two eddy currents are orthogonal in shape. While orthogonality is not expected in general, our results still show that patterned passive shield fundamentally changes the spatial/spectral footprint of the motional eddy current and can significantly reduce the leakage field in certain frequency bands and spatial regions. Larger leakage field peaks at certain frequencies may be reduced through structural reinforcements that target specific vibration modes. It should be noted that such measures as well as the cut-out patterns themselves depend on the driving (gradient) coil. This implies that in MRI with three gradient coils, three separate shielding layers are needed for coil specific shielding. In many cases, transverse (X and Y) gradient fields are stronger inducers of magnet heating than the longitudinal (Z) one, so two shields may suffice to address practical heating issues.

We emphasize that a reduction in the motional eddy current by means of cutting slits and patterns needs to be done judiciously to preserve the desired, shielding eddy currents. One method, different from ours, to do so would be to make cuts (slits) along the eddy image paths while not arranging the remaining conductor into a single loop. Such cuts, while indeed reducing the orthogonal eddy currents, will still allow multiple undesirable modes of surface currents to flow in response to motional EMF. Our method aimed to impose the most stringent blocking of unwanted currents by admitting only one current mode defined by the eddy image.

Motional eddy current can also occur in other metallic components in MRI such as gradient coils themselves and the cryostat. Eddy current (motional or not) in copper conductors of the gradient coil can be reduced by dividing the current-carrying wires into multiple longitudinal segments²³ or building the coil out of the Litz wire.²⁴ The cryostat and the metallic thermal shield can, in principle, benefit from our proposed method to selectively suppress motional eddy current. In practice, however, the requirement of separate cutting patterns for different gradient axes makes its implementation difficult on existing magnet structures. A multi-layer, add-on passive shield assembly appears to be the best candidate for the application of the proposed method.

This work has several limitations. First, the closed-form solutions [Eqs. (17) and (21)] were derived for an infinitely large plate and not applicable to a practical shield. For a finite-sized plate, the

operator solutions [Eqs. (13) and (20)] need to be numerically solved under specific boundary conditions. While this can be readily done with today's computing hardware, our initial survey indicated that the results are sensitive to the mechanical boundary condition applied to the copper plate. For the numerical solution to be useful, the boundary condition should be matched by the experimental setup. Our initial intention in setting up the shield in Fig. 4 was to realize a well-defined, clamped boundary condition for the copper plates, but subsequent vibration measurements indicated that this was not achieved as the aluminum frame was subject to significant vibration. Because of this difficulty, we decided not to pursue numerical analysis in this paper. We tried to highlight general conclusions that do not rely on the infinite plate assumption. For example, the positive definiteness of the inductance operator and possibility of negative motional inductance are valid at the operator level without an infinite size assumption. Furthermore, no such assumption was used in Secs. II B and II C on patterned conductive shield.

Second, most gradient coils and, therefore, envisioned passive shield layers are cylindrical. This further limits the utility of our flat-geometry equations. As the system becomes cylindrical, the most prominent change in the fundamental equations will be on the mechanical force operator \mathcal{F}_M [Eq. (3)]. Equation of motion of a cylindrical shell is known to be complex, especially for think-walled cases.¹⁷ It is unlikely that a closed-form solution similar to Eq. (17) can be obtained, and once again numerical solution will be important. It is our conjecture that the general form of the coupled equations (1) and (5) will be retained in non-flat geometries, which will then lead to an operator solution similar to Eq. (10) for a continuous shield and the current solution analogous to Eq. (37) for a patterned shield. Ascertaining the predictive power of such solutions for a realistic, cylindrical shield will be an important milestone of our theory.

Third, our thin-plate theory ignored current flowing within the thickness of the shield. For the copper plate used in the experiment, the skin depth becomes smaller than the thickness (1.6 mm) at about 1700 Hz. Therefore, the current can flow non-uniformly across the plate's thickness. In the frequency domain, the skin effect can be approximately captured by allowing the surface conductivity σ_s to vary with ω . At 3 kHz, this will reduce σ_s by about 25%. This does not affect Fig. 8(b), however, since the calculation was based on the measured impedance. Furthermore, at frequencies where the skin effect is important, the impedance of the eddy current modes is expected to be dominated by the inductive term, namely, $\omega L \gg R$, based on quick, order-of-magnitude estimation. This implies that a skin effect-induced, minor increase in resistance will not change our main results significantly.

Finally, we found experimentally that the patterned shield can in fact increase the leakage field near the center of the driving coil at certain frequencies. In particular, the main resonance peak at around 400 Hz is prominently increased around $z=0$ compared to the solid copper shield. One explanation is that in a solid conductive plate, the main resonant vibration is hindered by magnetic damping acting on concomitant, minor eddy current loops (modes), while patterned copper, by design, is largely devoid of such mechanism. The unwanted focal increase in the leakage field is clearly a challenge of the proposed

method and calls for independent (perhaps structural) mitigation measures to supplement it.

Any such measure will benefit from the reliable prediction of resonance frequencies and amplitudes. As explained above, our theory at this stage does not directly provide such prediction. We showed, however, that in-magnet impedance measurement of the patterned shield accurately predicts the measured leakage field (Fig. 8) through Eq. (50). In this regard, our theory does provide a guide to characterize the patterned shield and empirically optimize it to minimize leakage fields.

In conclusion, we have developed a theory of magneto-mechanical resonance in distributed current and demonstrated motional eddy current-modified passive shield of an AC magnetic field through mode-limiting cutouts made on a conductive plate. Our results can help develop methods to effectively control motion-induced eddy current and limit leakage field amplification in a strong static magnetic field environment. Such methods can be useful to minimize magnet–gradient interaction in high-field MRI scanners.

ACKNOWLEDGMENTS

The authors thank Eric Budesheim for his help with mechanical setup of the leakage field experiments. This work was supported, in part, by the U.S. National Institutes of Health under Grant No. U01EB026976. The paper does not necessarily represent the views of the funding agency.

AUTHOR DECLARATIONS

Conflicts of Interest

The authors are employed by GE HealthCare.

Author Contributions

Seung-Kyun Lee: Conceptualization (lead); Data curation (lead); Formal analysis (lead); Investigation (lead); Methodology (lead); Software (lead); Writing – original draft (lead); Writing – review & editing (lead). **Yihe Hua:** Conceptualization (supporting); Investigation (supporting); Methodology (supporting); Software (equal); Writing – review & editing (supporting).

DATA AVAILABILITY

The data that support the findings of this study are available from the corresponding author upon reasonable request.

APPENDIX A: DERIVATION OF THE COUPLED EQUATIONS

Equation of motion

We start from the following general equation of motion governing the mechanical response of the mass element $\rho_m dz dx$ subject to forces,

$$\rho_m \ddot{u} = f_M + f_L. \quad (\text{A1})$$

This corresponds to Newton's equation of motion $ma = F$ applied to vertical (y) displacement normalized to the unit area in the zx

plane. Here, f_M represents the plate's elastic restoring force and damping force, and f_L is the Lorentz force, per area. Soedel [Eqs. (4.4.19) and (8.1.2) of Ref. 17] lists the following expression for the restoring and damping forces for a thin plate:

$$f_M = -D\nabla^4 u - \lambda \dot{u}. \quad (\text{A2})$$

The Lorentz force under static field $B_0 \hat{z}$ applies to the surface current flowing in the x direction and can be written as

$$f_L = (\vec{j} \times B_0 \hat{z}) \cdot \hat{y} = -j_x B_0 = -\left(-\frac{\partial T}{\partial z} B_0\right) = B_0 \frac{\partial T}{\partial z}. \quad (\text{A3})$$

Combining the above three equations, we get

$$\rho_m \ddot{u} = -D\nabla^4 u - \lambda \dot{u} + B_0 \frac{\partial T}{\partial z}, \quad (\text{A4})$$

which becomes in the frequency domain, after rearranging terms,

$$D\nabla^4 u + i\omega\lambda u - \rho_m \omega^2 u = B_0 \frac{\partial T}{\partial z}. \quad (\text{A5})$$

This concludes the derivation of Eq. (1).

Circuit equation

Next, we consider the circuit equation governing T . We start from Maxwell's induction equation $\nabla \times \vec{E} = -\partial \vec{B}/\partial t$. Taking a dot product with the surface-normal vector, we have

$$(\nabla \times \vec{E}) \cdot \hat{n} = -\frac{\partial B_\perp}{\partial t}. \quad (\text{A6})$$

For a conductive plate with thickness h and bulk conductivity σ , the E field is related to the surface current density by $\vec{j} = h\vec{j} = \sigma h \vec{E} = \sigma_s \vec{E}$, where σ_s is the surface conductivity. Further using the expression $\vec{j} = \nabla \times (T\hat{n})$, we can rewrite the left-hand side of the above equation as

$$\begin{aligned} (\nabla \times \vec{E}) \cdot \hat{n} &= \sigma_s^{-1} (\nabla \times \nabla \times (T\hat{n})) \cdot \hat{n} \\ &= \sigma_s^{-1} (\nabla(\nabla \cdot (T\hat{n})) - \nabla^2(T\hat{n})) \cdot \hat{n} = -\sigma_s^{-1} \nabla^2 T. \end{aligned} \quad (\text{A7})$$

In the above, we used the fact that T does not vary along \hat{n} , which leads to the zero divergence of $T\hat{n}$ (in Cartesian coordinates) and also that the vector Laplacian amounts to the Laplacian on each Cartesian component. From Eqs. (A6) and (A7), we obtain what we can call a "surface eddy current equation,"

$$\frac{\partial B_\perp}{\partial t} = \sigma_s^{-1} \nabla^2 T. \quad (\text{A8})$$

Incidentally, this equation can be shown to hold for cylindrical and spherical surface currents as well.

The normal magnetic field B_\perp consists of three parts: applied field B_{app} , self-induced field B_{self} that depends on T , and motional field B_{motion} that depends on u . That is,

$$B_\perp = B_{app} + B_{self}\{T\} + B_{motion}\{u\}. \quad (\text{A9})$$

In light of the dipole density interpretation¹⁸ of T , the self-induced field at location (z, x) can be obtained by integrating the dipolar field contributions of T at locations (z', x') . Symbolically,

$$B_{self}(z, x, t) = \iint K(z, x; z', x') T(z', x', t) dz' dx' \equiv K^* T(z, x, t), \quad (\text{A10})$$

where we denoted by K the dipolar field kernel that links the surface-normal dipoles to surface-normal magnetic fields.

The relationship between u and B_{motion} comes from projecting the tilted area element of the displacement field $u(z, x)$ with gradient $\nabla u = (\partial u/\partial z, \partial u/\partial x)$ along the \hat{z} direction. The projection equals (details omitted)

$$da_{proj} = -\frac{\partial u}{\partial z} dz dx. \quad (\text{A11})$$

The negative sign signifies that when u tilts down toward $+\hat{z}$, it receives positive (upward) penetration of B_0 flux, $d\Phi_{motion} = B_0 \cdot da_{proj}$. By dividing this flux with $dz dx$, we get the motional field,

$$B_{motion}\{u\} = -B_0 \frac{\partial u}{\partial z}. \quad (\text{A12})$$

Combining Eqs. (A8)–(A10), and (A12), we finally obtain the circuit equation,

$$\frac{\partial B_{app}}{\partial t} + K^* \frac{\partial T}{\partial t} - B_0 \frac{\partial}{\partial z} \frac{\partial u}{\partial t} = \sigma_s^{-1} \nabla^2 T, \quad (\text{A13})$$

which becomes in the frequency domain, after rearranging terms,

$$-\sigma_s^{-1} \nabla^2 T + i\omega K^* T - i\omega B_0 \frac{\partial u}{\partial z} = -i\omega B_{app}. \quad (\text{A14})$$

This is Eq. (5). Note that no assumption of an infinite plane was used in Eqs. (A5) and (A14).

For an infinitely large flat surface, the operator K^* is diagonal in the Fourier domain; a plane wave dipolar density produces a matched plane wave normal magnetic field with a wavevector-dependent eigenvalue. The mathematical expression for the eigenvalue can be found from Ref. 15, whose Eqs. (18) and (21) list a T basis function (2D plane wave) and the corresponding normal magnetic field, respectively, on two different planes separated by $z - z_0$. In the limit of $z - z_0 \rightarrow 0$, Ref. 15 gives the following eigenvalue:

$$K^* \leftrightarrow \frac{\mu_0}{2} k \text{ (Infinite plate)}, \quad (\text{A15})$$

where μ_0 is the permeability in vacuum and $k = |\vec{k}|$ is the magnitude of the 2D wavevector.

APPENDIX B: MAGNETIC DAMPING AND STIFFENING

Suppose our conductive plate is driven by a mechanical force F_{ext} instead of an applied magnetic field. The two coupled

equations [Eqs. (1) and (5)] are modified as

$$\mathcal{A}u = \mathcal{B}T + F_{ext}, \quad (B1)$$

$$\mathcal{C}T + \mathcal{D}u = 0. \quad (B2)$$

Equation (B2) can be formally solved for T and substituted in Eq. (B1) to eliminate T ,

$$\mathcal{A}u = -\mathcal{B}\mathcal{C}^{-1}\mathcal{D}u + F_{ext}. \quad (B3)$$

Explicitly,

$$(-\mathcal{F}_M - \rho_m\omega^2)u = i\omega B_0^2 \frac{\partial}{\partial z} (-\sigma_s^{-1}\nabla^2 + i\omega K^*)^{-1} \frac{\partial}{\partial z} u + F_{ext}. \quad (B4)$$

While this is not immediately illuminating, its significance can be appreciated when we consider the following two cases.

Magnetic damping

If the resistive term in \mathcal{C} dominates the inductive term, for example, when $\sigma_s \rightarrow 0$ or $\omega \rightarrow 0$, Eq. (B4) becomes

$$(-\mathcal{F}_M - \rho_m\omega^2)u = -i\omega B_0^2 \sigma_s^{-1} \frac{\partial}{\partial z} (\nabla^2)^{-1} \frac{\partial}{\partial z} u + F_{ext}. \quad (B5)$$

We note that the magneto-mechanical term (first term on the right-hand side) is purely imaginary or 90° shifted from the inertia term. When transferred to the left, it adds to the mechanical damping term $i\omega\lambda u$ contained in $-\mathcal{F}_M u$. We can, therefore, define a magnetic damping operator,

$$\mathcal{G} \equiv B_0^2 \sigma_s^{-1} \frac{\partial}{\partial z} (\nabla^2)^{-1} \frac{\partial}{\partial z}, \quad (B6)$$

and rewrite Eq. (B5) as

$$(-\mathcal{F}_M + i\omega\mathcal{G} - \rho_m\omega^2)u = F_{ext}, \quad (B7)$$

from which the role of the damping term is clearer. Note that \mathcal{G} is proportional to B_0^2 and is positive semi-definite; in the Fourier domain (finite or infinite), it reduces to $B_0^2 \sigma_s^{-1} k_z^2/k^2 \geq 0$. Physically, magnetic damping of a conductive plate results from the bending of the plate (du/dz) cutting the flux lines of $B_0\hat{z}$, triggering Lorentz force in the form of motional EMF, which, in turn, causes surface current to flow, which then is subject to another Lorentz force acting on the plate in a way to suppress motion. In this process, 90° phase shift (time derivative) occurs once between the displacement (du/dz) and the motional EMF.

Magnetic stiffening

If the inductive term dominates \mathcal{C} as in $\sigma_s \rightarrow \infty$ or $\omega \rightarrow \infty$, the magneto-mechanical term becomes real and Eq. (B4) is approximated as

$$(-\mathcal{F}_M - \rho_m\omega^2)u = B_0^2 \frac{\partial}{\partial z} (K^*)^{-1} \frac{\partial}{\partial z} u + F_{ext}. \quad (B8)$$

The magneto-mechanical term is again proportional to B_0^2 and contains $\partial u/\partial z$ corresponding to the plate's bending in the B_0 direction. This term opposes the plate's motion in the following sense. Let us define the first term on the right-hand side of Eq. (B8) as $-\mathcal{S}u$ where

$$\mathcal{S} \equiv -B_0^2 \frac{\partial}{\partial z} (K^*)^{-1} \frac{\partial}{\partial z}. \quad (B9)$$

Because the inductance operator K^* [Eq. (9)] is positive definite, its inverse also is. It follows that for any displacement field $u(z, x)$ that satisfies zero or periodic boundary condition in z , the integral (with limits defining the boundary)

$$\int_{z_1}^{z_2} -u \frac{\partial}{\partial z} (K^*)^{-1} \frac{\partial u}{\partial z} dz = \int_{z_1}^{z_2} \frac{\partial u}{\partial z} (K^*)^{-1} \frac{\partial u}{\partial z} dz \quad (B10)$$

is non-negative. Therefore, the operator [Eq. (B9)] is positive semi-definite and we can regard $-\mathcal{S}u$ as a form of restoring force as in Hooke's spring law $F = -k_H x$. Given this consideration, we may call \mathcal{S} the magnetic stiffening operator and rewrite Eq. (B8) as

$$(-\mathcal{F}_M + \mathcal{S} - \rho_m\omega^2)u = F_{ext}. \quad (B11)$$

In practice, both terms in \mathcal{C} are present, and magneto-mechanical suppression of motion has both in-phase and out-of-phase components (with respect to the inertia term). That is, magnetic damping and stiffening co-exist in general, both being proportional to B_0^2 .

APPENDIX C: DERIVATION OF RESISTANCE, INDUCTANCE, AND MAGNETIC FLUX EXPRESSIONS

First, we note that if $B_{app}(z, x)$ is the normal magnetic field on the plate where a surface coil is patterned according to the number-of-turns function $N(z, x) = \tilde{T}_{eddyi}$, then $\iint \tilde{T}_{eddyi} B_{app} dz dx$ corresponds to the flux picked up by the coil. This can be understood by dividing \tilde{T}_{eddyi} into a collection of series-connected small solenoidal loops covering the plate whose turn-counts and areas are given by $\tilde{T}_{eddyi}(z, x)$ and $dz dx$, respectively. The total flux in the coil is then given by the integral Eq. (29).

Now if the loop carries a current I , the self-generated normal magnetic field is $B_{\perp} = K^* \tilde{T}_{eddyi} I$ by definition of the operator K^* . The flux picked up by the same loop, divided by I , is then given by the integral of Eq. (28). This is the self-inductance of the loop.

Last, Eq. (27) can be proven as follows. At the boundary of the shield plate, the number-of-turns function is zero by definition: $\tilde{T}_{eddyi} = 0$ (plate boundary). Consider a vector field defined in the zx plane, $\vec{V} \equiv \tilde{T}_{eddyi} \nabla \tilde{T}_{eddyi}$. Since this is also zero at the boundary, we can say $\oint \vec{V} \cdot \hat{n} dl = 0$ where the integral is along the boundary and \hat{n} is the unit normal vector at the boundary. From the two-dimensional divergence theorem, this integral equals

$$\oint \vec{V} \cdot \hat{n} dl = \iint \nabla \cdot \vec{V} dz dx, \quad (C1)$$

which expands as

$$\begin{aligned} \iint \nabla \cdot \tilde{\mathbf{V}} dz dx &= \iint \nabla \cdot (\tilde{T}_{eddyi} \nabla \tilde{T}_{eddyi}) dz dx \\ &= \iint \nabla \tilde{T}_{eddyi} \cdot \nabla \tilde{T}_{eddyi} dz dx + \iint \tilde{T}_{eddyi} \nabla^2 \tilde{T}_{eddyi} dz dx = 0. \end{aligned} \quad (C2)$$

Therefore, the left-hand side of Eq. (27) is

$$-\sigma_s^{-1} \iint \tilde{T}_{eddyi} \nabla^2 \tilde{T}_{eddyi} dz dx = \sigma_s^{-1} \iint \nabla \tilde{T}_{eddyi} \cdot \nabla \tilde{T}_{eddyi} dz dx. \quad (C3)$$

The fact that this equals the coil's resistance comes from the following consideration. If the coil carries current I , the surface current density vector $\vec{j}(z, x)$ is given by

$$\vec{j} = \left(\frac{\partial \tilde{T}_{eddyi}}{\partial x} \hat{z} - \frac{\partial \tilde{T}_{eddyi}}{\partial z} \hat{x} \right) I \quad (C4)$$

from the relation $\vec{j} = \nabla \times (\tilde{T}_{eddyi} I \hat{y})$. This implies that the magnitude of the surface current density is related to $\nabla \tilde{T}_{eddyi}$ as

$$|\vec{j}|^2 = I^2 \nabla \tilde{T}_{eddyi} \cdot \nabla \tilde{T}_{eddyi}. \quad (C5)$$

The total Joule heating of the coil equals the surface integral of the power density, $\sigma_s^{-1} |\vec{j}|^2$, as

$$P = \sigma_s^{-1} \iint |\vec{j}|^2 dz dx = \sigma_s^{-1} I^2 \iint \nabla \tilde{T}_{eddyi} \cdot \nabla \tilde{T}_{eddyi} dz dx. \quad (C6)$$

Equating this with $P = I^2 R$, we get Eq. (27).

REFERENCES

- ¹L. Jiang, Y. Hua, L. Ma, S. Moon, J. Li, K. Mogatadakala, and T. Havens, in *22nd Annual Meeting of ISMRM* (International Society of Magnetic Resonance in Medicine, Milan, 2014), Abstract 4846.
- ²Y. Hua, L. Jiang, G. C. McKinnon, S.-K. Lee, and A. Wu, in *20th Annual Meeting of ISMRM* (International Society of Magnetic Resonance in Medicine, Melbourne, 2012), 2012), Abstract 2580.
- ³M. Rausch, M. Gebhardt, M. Kaltenbacher, and H. Landes, *IEEE Trans. Magn.* **41**(1), 72–81 (2005).
- ⁴S. A. Winkler, F. Schmitt, H. Landes, J. de Bever, T. Wade, A. Alejski, and B. K. Rutt, *Neuroimage* **168**, 59–70 (2018).
- ⁵N. Boulant, L. Quettier, and C. Iseult, *Magn. Reson. Mater. Phys. Biol. Med.* **36**(2), 175–189 (2023).
- ⁶N. Boulant, C. Le Ster, A. Amadon, G. Aubert, A. Beckett, J. Belorgey, C. Bonnelye, D. Bosch, D. O. Brunner, G. Dilasser, O. Dubois, P. Ehses, D. Feinberg, S. Feizollah, V. Gras, S. Gross, Q. Guihard, H. Lannou, D. Le Bihan, F. Mauconduit, F. Molinié, F. Nunio, K. Pruessmann, L. Quettier, K. Scheffler, T. Stöcker, C. Tardif, K. Ugurbil, A. Vignaud, A. Vu, and X. Wu, *Magn. Reson. Mater. Phys. Biol. Med.* **37**, 169–183 (2024).
- ⁷P. B. Roemer and W. A. Edelstein, in *Fifth Annual Meeting of the Society of Magnetic Resonance in Medicine* (International Society of Magnetic Resonance in Medicine, Montreal, Quebec, 1986), p. 1067.
- ⁸G. B. J. Mulder, C. L. G. Ham, A. J. Mateboer, N. B. Roozen, and J. P. M. Verbunt, Patent US 6,326,788 B1 (2001).
- ⁹M. Westphal, U.S. patent 7,514,928 B2 (2009).
- ¹⁰J.-B. Mathieu, E. T. Laskaris, K. W. Rohling, M. Xu, and S.-K. Lee, U.S. patent 10,281,538 B2 (2019).
- ¹¹E. T. Laskaris, L. Jiang, and Y. Hua, U.S. patent 10,416,254 B2 (2019).
- ¹²T. K.-F. Foo, M. Vermilyea, G. Conte, C. V. Epps, J. Ricci, M. Xu, A. Wu, S. Huang, S.-K. Lee, W. Stautner, Y. Bai, D. Kelley, J. Huston III, M. A. Bernstein, Y. Shu, C. Hess, and D. Xu, in *31st Annual Meeting of ISMRM* (International Society of Magnetic Resonance in Medicine, Toronto, ON, 2023), Abstract 4586.
- ¹³S.-K. Lee and M. A. Bernstein, *Magn. Reson. Med.* **88**(4), 1901–1911 (2022).
- ¹⁴R. Turner and R. M. Bowley, *J. Phys. E* **19**, 876–879 (1986).
- ¹⁵S.-K. Lee and J. Schenck, *J. Appl. Phys.* **133**, 174504 (2023).
- ¹⁶L. Jiang and T. J. Havens, *IEEE Trans. Appl. Supercond.* **22**(3), 4400704 (2012).
- ¹⁷W. Soedel, *Vibrations of Shells and Plates*, 3rd edition (Taylor & Francis, Boca Raton, 2004).
- ¹⁸A. J. Mäkinen, R. Zetter, J. Iivanainen, K. C. Zevenhoven, L. Parkkonen, and R. J. Ilmoniemi, *J. Appl. Phys.* **128**(6), 063906 (2020).
- ¹⁹J. F. Schenck, M. A. Hussain, and W. A. Edelstein, U.S. patent 4,646,024 (1987).
- ²⁰R. Shankar, *Principles of Quantum Mechanics* (Plenum Press, New York, 1994).
- ²¹S.-K. Lee, in *31st Annual Meeting of ISMRM* (International Society of Magnetic Resonance in Medicine, Toronto, 2023), Abstract 4560.
- ²²E. Motovilova and S. A. Winkler, *Front. Phys.* **10**, 907619 (2022).
- ²³D. A. Feinberg, A. J. S. Beckett, A. T. Vu, J. Stockmann, L. Huber, S. Ma, S. Ahn, K. Setsompop, X. Cao, S. Park, C. Liu, L. L. Wald, J. R. Polimeni, A. Mareyam, B. Gruber, R. Stirnberg, C. Liao, E. Yacoub, M. Davids, P. Bell, E. Rummert, M. Koehler, A. Potthast, I. Gonzalez-Insua, S. Stocker, S. Gunamony, and P. Dietz, *Nat. Methods* **20**, 2048–2057 (2023).
- ²⁴B. A. Chronik, A. Alejski, and B. K. Rutt, *Magn. Reson. Med.* **44**, 955–963 (2000).